

A Systematic Study of the Structural and Magnetic Properties of Mn-, Co-, and Ni-Doped Colloidal Magnetite Nanoparticles

Francis Leonard Deepak,[†] Manuel Bañobre-López,[†] Enrique Carbó-Argibay,[†] M. Fátima Cerqueira,[‡] Yolanda Piñeiro-Redondo,[§] José Rivas,[§] Corey M. Thompson,^{||} Saeed Kamali,[⊥] Carlos Rodríguez-Abreu,[†] Kirill Kovnir,[⊥] and Yury V. Kolen'ko^{*,†}

[†]International Iberian Nanotechnology Laboratory, Braga 4715-330, Portugal

[‡]Center of Physics, University of Minho, Braga 4710-057, Portugal

[§]Department of Applied Physics, University of Santiago de Compostela, Santiago de Compostela 15782, Spain

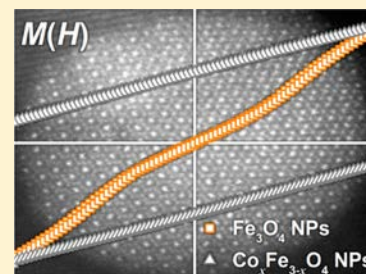
^{||}Department of Chemistry and Brockhouse Institute of Materials Research, McMaster University, Hamilton, Ontario L8S 4M1, Canada

[⊥]Department of Chemistry, University of California, Davis, Davis, California 95616, United States

Supporting Information

ABSTRACT: A series of colloidal $M_xFe_{3-x}O_4$ ($M = Mn, Co, Ni; x = 0-1$) nanoparticles with diameters ranging from 6.8 to 11.6 nm was synthesized by hydrothermal reaction in aqueous medium at low temperature (200 °C). Energy-dispersive X-ray microanalysis and inductively coupled plasma spectrometry confirm that the actual elemental compositions agree well with the nominal ones. The structural properties of the obtained nanoparticles were investigated by powder X-ray diffraction, Raman spectroscopy, Mössbauer spectroscopy, X-ray and neutron pair distribution function analysis, and electron microscopy. The results demonstrate that our synthesis technique leads to the formation of chemically uniform single-phase solid solution nanoparticles with cubic spinel structure, confirming intrinsic doping. The local structure of the Fe_3O_4 NPs is distorted with respect

to the cubic inverse-spinel structure, while chemical substitution of Fe by Mn or Ni partially eliminates the local distortions. Magnetic studies showed that, in comparison to nondoped Fe_3O_4 , the saturation magnetization (M_s) of $M_xFe_{3-x}O_4$ ($M = Mn, Ni$) decreases with increasing dopant concentration, while Co-doped samples showed similar M_s . On the other hand, whereas Mn- and Ni-doped nanoparticles exhibit superparamagnetic behavior at room temperature, ferrimagnetism emerges for $Co_xFe_{3-x}O_4$ nanoparticles, which can be tuned by the level of Co doping.



1. INTRODUCTION

Magnetite, Fe_3O_4 , is an iron oxide with an inverse-spinel crystal structure of AB_2O_4 type, $(Fe^{3+})^A[Fe^{2+}Fe^{3+}]^B O_4$.¹ Bulk Fe_3O_4 is crystallized in the cubic space group $Fd-3m$ with the unit cell parameter $a \approx 8.4$ Å. Two geometrically different cation sites are present in the crystal structure: A sites are tetrahedrally coordinated by O atoms and are occupied exclusively by Fe^{3+} cations, while B sites are octahedrally coordinated by O atoms and are occupied by an equal number of Fe^{2+} and Fe^{3+} cations. Charge ordering of Fe^{2+} and Fe^{3+} and the associated local structural distortion was proposed by Verwey in 1939² and recently validated by Atfield and coauthors.³

From the nanoscience point of view, Fe_3O_4 is a classic example of a system demonstrating a finite size effect, wherein the magnetic properties of the bulk material are different from its nanosized counterpart. More specifically, at room temperature (RT), a bulk multidomain ferrimagnet (FiM) is transformed to a single-domain FiM upon particle size reduction below 80 nm, and then further converted into a superparamagnet (SPM) by particle size reduction below 25 nm.⁴

The SPM Fe_3O_4 nanoparticles (NPs) typically exhibit high saturation magnetization (M_s) and high Curie temperature (T_C).⁴ They can be prepared in the form of solution-based colloidal dispersions, which are stable for long periods of time. The combination of these properties makes colloidal SPM Fe_3O_4 NPs particularly attractive for many advanced medical applications, such as magnetic resonance imaging, magnetically guided/induced drug delivery, and cancer therapy via NP-mediated magnetic hyperthermia.⁵

Apart from tuning of the properties of Fe_3O_4 by changing the particle size, modification of the intrinsic properties can be achieved by chemical doping. In bulk form, iron cations in Fe_3O_4 can be readily substituted by a number of divalent, trivalent, and tetravalent cations while maintaining the spinel structure, as it is known to occur naturally in minerals.⁶ The products of such doping range from magnetites with low levels of isomorphic substitution up to fully substituted MFe_2O_4 (ferrites). In the bulk Fe_3O_4 , which demonstrates the FiM

Received: February 16, 2015

Revised: April 27, 2015

Published: April 28, 2015

behavior, all Fe^{3+} cations, equally distributed in A and B sublattices, are antiferromagnetically (AFM) coupled, thereby effectively negating each other. In contrast, uncompensated unpaired electrons of the Fe^{2+} cations in the B sublattice are responsible for the observed high magnetic moment of bulk Fe_3O_4 .⁷ Hastings and coauthors have investigated the structural changes in a series of transition-metal (TM) doped Fe_3O_4 and have shown that Mn^{2+} has a tendency to replace Fe^{3+} in AO_4 tetrahedra, while Co^{2+} and Ni^{2+} tend to replace $\text{Fe}^{3+}/\text{Fe}^{2+}$ in BO_6 octahedra.⁸ The intrinsic magnetic properties of Fe_3O_4 can be altered by elemental substitution on both A and B sites in the inverse-spinel AB_2O_4 structure type. In this regard, the exploration and in-depth understanding of the changes in the structure and magnetic properties of Fe_3O_4 NPs as a function of gradual TM doping is of high interest from both fundamental and technological points of view.

Notably, doping of Fe_3O_4 is primarily investigated for thin film samples and typically affects the structural, magnetic, and transport properties of the corresponding magnetite-based materials.^{9–13} For example, systematic increase of the cobalt content in $\text{Co}_x\text{Fe}_{3-x}\text{O}_4$ films drastically raises the coercivity and decreases magnetoresistance and saturation magnetization.^{10–12} At the same time, very little is known about the effects of doping for isotropic colloidal NPs of magnetite.^{14,15}

The synthesis of NPs with effective dopant incorporation into the crystal structure is a nontrivial task due to thermodynamic reasons.^{16,17} NPs have a thermodynamic preference to expel dopants from the structure to minimize the overall free energy, i.e., the so-called self-purification phenomenon.^{18,19} Additionally, compositionally complex NPs can exhibit a tendency for phase separation, thus forming secondary phases, which are also more favorable from a thermodynamic point of view. The solution-based synthesis methods developed for colloidal NPs, however, rely largely on kinetic factors, which allow the aforementioned thermodynamic issues to be overcome and successfully incorporate dopants into the NP structure. The thermal decomposition approach has been demonstrated to be the most successful one for the synthesis of doped colloidal Fe_3O_4 NPs in terms of magnetic properties.²⁰ This technique, however, is inconvenient due to utilization of flammable organic solvents at high temperatures (300 °C) and is also restricted to small yields.²¹ Therefore, a robust method offering high quality doped NPs is highly desirable.

In the present study, we report the low-temperature hydrothermal synthesis of $\text{M}_x\text{Fe}_{3-x}\text{O}_4$ ($\text{M} = \text{Mn}, \text{Co}, \text{Ni}; x = 0–1$) colloidal NPs. The preparation has been realized in aqueous medium under comparatively mild conditions avoiding high-temperature syntheses in organic solvent. We show that, in this synthesis, the nondoped and doped NPs are single phases exhibiting an average particle diameter in the range 7–12 nm. Furthermore, our detailed characterization has proved the interstitial substitution of the iron cations by the dopants, forming compositionally uniform particles. We have also explored the magnetic behavior of the as-synthesized NPs as a function of Mn, Co, and Ni doping observing a change from SPM to FiM at room temperature with increasing Co content in $\text{Co}_x\text{Fe}_{3-x}\text{O}_4$ NPs.

2. EXPERIMENTAL SECTION

Colloidal Fe_3O_4 NPs and a series of doped $\text{M}_x\text{Fe}_{3-x}\text{O}_4$ ($\text{M} = \text{Mn}, \text{Co}, \text{Ni}$) NPs were synthesized according to our previously reported hydrothermal method;²² a detailed synthesis proce-

cedure is described in the Supporting Information. The products were characterized by energy-dispersive X-ray spectroscopy using scanning electron microscopy (SEM–EDX) (Quanta 650 FEG ESEM, FEI – INCA 350 spectrometer, Oxford Instruments), inductively coupled plasma–optical emission spectroscopy (ICP–OES) (ICPE-9000 spectrometer, Shimadzu), powder X-ray diffraction (XRD) (X'Pert PRO diffractometer, PANalytical),²³ Raman spectroscopy (alpha300 R confocal microscope, WITec), ⁵⁷Fe Mössbauer spectroscopy,²⁴ neutron and X-ray pair distribution function analysis (PDF) (Nano-scale-Ordered Materials Diffractometer (NOMAD) at the ORNL's Spallation Neutron Source and beamline 11-ID-B at the ANL's Advanced Photon Source),²⁵ transmission electron microscopy (TEM), high-resolution TEM (HRTEM), high-angle annular dark-field scanning TEM (HAADF–STEM), EDX and electron energy loss spectroscopy (EELS) in STEM mode (Titan ChemiSTEM 80–200 kV, FEI), vibrating sample magnetometry (VSM) (EV7, MicroSense), and magnetization measurements (SQUID-VSM magnetometer, Quantum Design). For more details regarding characterization, see the Supporting Information.

3. RESULTS AND DISCUSSION

Synthesis. Colloidal NPs of $\text{M}_x\text{Fe}_{3-x}\text{O}_4$ ($\text{M} = \text{Mn}, \text{Co}, \text{Ni}; x = 0, 0.06, 0.15, 0.3, 0.6, 0.9, \text{ and } 1$) were prepared in aqueous reaction medium using a modified hydrothermal method with oleate as a surfactant.^{22,26} The role of the surfactant is to provide colloidal stability to the NPs and to regulate their growth. Chloride salts of Fe^{3+} , Fe^{2+} , Mn^{2+} , Co^{2+} , and Ni^{2+} were used as precursors, and concentrated NH_4OH was used as a precipitation agent. The temperature and the duration of hydrothermal treatment were optimized to ensure the formation of NPs with a relatively narrow size distribution around 10 nm.

Composition. SEM–EDX analysis of the samples reveals that the actual elemental compositions of the $\text{M}_x\text{Fe}_{3-x}\text{O}_4$ NPs agree well with the nominal composition used for NP synthesis, demonstrating good control of the composition by our hydrothermal method. Several randomly selected areas from each sample were analyzed by SEM–EDX, showing a uniform distribution of the constituent elements. ICP–OES analysis of the selected samples shows that the final compositions of the synthesized NPs are in good agreement with the nominal compositions, wherein the deviations between the nominal and analytically determined compositions of all tested samples were found to be smaller than 0.3 at. %. Hence, the nominal chemical composition of the as-synthesized samples will be used in the following discussion.

Structure. XRD. According to the XRD analysis, all $\text{M}_x\text{Fe}_{3-x}\text{O}_4$ samples are single-phase nanopowders having the cubic inverse-spinel structure type (S. G.: $Fd-3m$, no. 227). No diffraction peaks corresponding to secondary phases or other impurities were detected in the XRD patterns. Despite the broadening of the XRD peaks due to small particle sizes, reliable unit cell parameters have been extracted using Ge as an internal standard (Figure 1, Table S1, Supporting Information). For the nondoped Fe_3O_4 NPs, the unit cell parameter a was established to be 8.356(2) Å. Although the value is slightly lower than that of bulk Fe_3O_4 (8.38–8.42 Å), this value is in good agreement with $a = 8.35$ Å reported for nanosized Fe_3O_4 .²⁷ As expected, the unit cell expansion in response to Mn doping was observed for the Mn-doped samples, since bulk MnFe_2O_4 has a larger unit cell (8.49–8.51 Å) compared to bulk

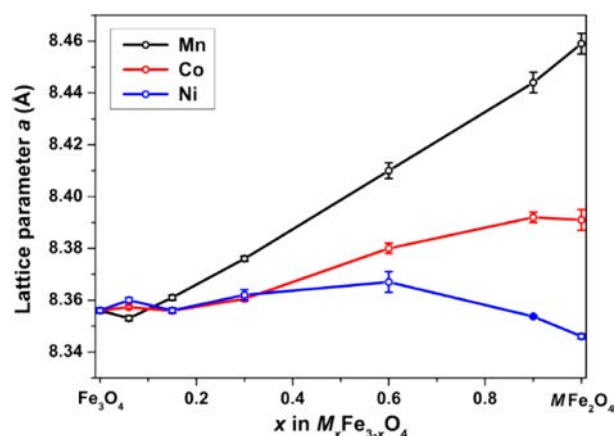


Figure 1. Lattice parameters of the $M_x\text{Fe}_{3-x}\text{O}_4$ ($M = \text{Mn}, \text{Co}, \text{Ni}$) obtained by least-squares refinements of the powder diffraction data. For some stoichiometries, error bars are smaller than the symbols.

Fe_3O_4 (Figure 1). For Ni- and Co-doped samples, no increase of the unit cell parameter is expected, since parameters for bulk phases are either lower, NiFe_2O_4 (8.33–8.34 Å), or similar, CoFe_2O_4 (8.37–8.39 Å), to those of bulk Fe_3O_4 . Both Co- and Ni-doped samples exhibit deviation from simple Vegard behavior. Alloying x from 0 to 0.6 in $M_x\text{Fe}_{3-x}\text{O}_4$ NPs produces a gradual increase of the unit cell parameter with increasing Co and Ni concentrations. For the more heavily doped samples ($x > 0.6$), in the case of the Ni-doping series, the parameter starts to decrease reaching $a = 8.346(1)$ Å for the NiFe_2O_4 end member, while Co-doping samples exhibit an increase of the unit cell parameter reaching $a = 8.391(4)$ Å for the CoFe_2O_4 end member. The observed deviations from Vegard behavior can be partly attributed to the different cation distribution in as-synthesized nanocrystalline samples as compared to the bulk ferrites.²⁸ This could also be due to local distortions in the AO_4 tetrahedra and BO_6 octahedra in the doped spinel structures, as reported previously.^{29,30} Although XRD results confirm the formation of a solid solution based on the magnetite structure with an increase of cubic parameter a , conventional XRD is not sensitive to small local distortions, which were investigated by synchrotron powder X-ray and neutron diffraction PDF (*vide infra*).

Raman Spectroscopy. Raman spectroscopy experiments were performed to further understand the structural changes of the host Fe_3O_4 matrix upon doping (Table S1 and Figure S1, Supporting Information). Analysis of the Raman data recorded for all as-synthesized NPs confirms that the Mn, Co, and Ni dopants fully dissolve in the magnetite, forming solid solutions $M_x\text{Fe}_{3-x}\text{O}_4$ with stoichiometric ferrites as the end members at $x = 1$.^{31–40} The results of Raman spectroscopy studies are in good agreement with the XRD results above.

Notably, the Raman data provide evidence of gradual and slight structural modification of the magnetite with chemical doping by Co and Ni, retaining an inverse-spinel type structure.⁴¹ In contrast, for the Mn-doped magnetite samples, the appearance of a new broad mode reveals a strong influence of this dopant on the host matrix. Observed changes in the Fe_3O_4 structure with Mn substitution are most likely a result of the increasing fingerprint from Mn–O bonds related to the local preferential distribution of Mn atoms in $M_n\text{Fe}_{3-n}\text{O}_4$, as hinted by Mössbauer spectroscopy. More details about Raman spectroscopy are provided in the Supporting Information.

Mössbauer Spectroscopy. Mössbauer spectra for parent compound Fe_3O_4 have two components above the Verwey transition temperature,² which is about 120 K for bulk Fe_3O_4 . Above this temperature, one signal is from Fe^{3+} located at the tetrahedral sites (A), and the other is from $\text{Fe}^{2.5+}$, which is the average of Fe^{3+} and Fe^{2+} located at the octahedral sites (B), with one electron hopping between them. The ratio of the A and B sites is 1:2. For the ferrite with TMs incorporated into the magnetite system, depending on the cation distributions, the Mössbauer signals can vary. In an ideal inverse ferrite assuming all M atoms occupied an octahedral site, the composition $(\text{Fe}_1)^{\text{A}}[\text{M}_1\text{Fe}_1]^{\text{B}}\text{O}_4$ is expected. In a normal ferrite assuming all M atoms occupied a tetrahedral site, the composition $(\text{M}_1)^{\text{A}}[\text{Fe}_2]^{\text{B}}\text{O}_4$ is expected. The ferrites' compositions shown below are calculated on the basis of the ratio of Fe atoms in octahedral and tetrahedral sites, which can vary theoretically from 1:1 for an ideal inverse ferrite to 0:2 for an ideal normal ferrite. The accuracy of such assignments can be estimated as $\pm 10\%$ taking into account the complicated overlapping spectra and possible surface layer contribution.⁴²

In none of the measured spectra of $M\text{Fe}_2\text{O}_4$ NPs ($M = \text{Mn}, \text{Co}, \text{Ni}$) there is any signal characteristic for Fe^{2+} with high centroid shift, $\delta > 0.6 \text{ mm s}^{-1}$. In turn, in the spectra of the parent Fe_3O_4 NP sample, the Fe^{2+} component with $\delta = 0.88 \text{ mm s}^{-1}$ was observed.⁴² This indicates that the incorporated TMs are all in the +2 oxidation state, and thus all the remaining ferrite iron atoms are in the Fe^{3+} oxidation state to keep overall neutrality. Although in general the hyperfine parameters for Fe^{3+} in the tetrahedral and octahedral sites are very close, the δ for the octahedral one is slightly higher due to longer Fe–O distances. It is worth mentioning that the B–A interaction is much stronger than the A–A interaction, and the B–B interaction can be neglected.⁴¹

The results observed at RT and 80 K are similar taking into account the narrowing of the line at lower temperature and the second order doppler (SOD) shift leading to increase of the δ values. Below, the 80 K data are discussed. The RT results are presented in the Supporting Information (pp. S2–S3, Table S2, Figure S2). All the hyperfine parameters extracted from the 80 K measurements are summarized in Table 1, while the corresponding spectra are given in Figure 2.

MnFe_2O_4 . This spectrum can be fitted with four magnetically split sextets. The relatively low δ values of the first two components, Q_1 and Q_2 , tempted us to assign them to Fe atoms in the tetrahedral A sites. The centroid shifts for these positions are 0.44 and 0.42 mm s^{-1} , and the hyperfine fields are 53.1 and 51.4 T. It is worth mentioning that the lower B_{hf} are characteristic of NPs due to the collective magnetic excitations (CMEs).^{43,44} The intensities for the first two components are 13 and 32%. Results of spectra fitting indicate that the total ratio of Fe in tetrahedral and octahedral positions is 45:55, resulting in the conclusion that the cation distribution is $(\text{Mn}_{0.1}\text{Fe}_{0.9})^{\text{A}}[\text{Mn}_{0.9}\text{Fe}_{1.1}]^{\text{B}}\text{O}_4$. Hence, most of the Mn atoms reside in octahedral positions.

Two types of Fe atoms were detected in octahedral positions (Q_3 and Q_4), where the centroid shifts are higher (ca. 0.51 mm s^{-1}) than Fe atoms in tetrahedral positions. The B_{hf} for the tetrahedral Fe atoms is higher than hyperfine field for Fe atoms in octahedral sites. This is in contrast to previous works,^{45,46} where some of the B-site Fe atoms had the highest B_{hf} . The reason for having a slightly higher B_{hf} for the Fe atoms in the A sites is an indication of the nonuniform distribution of Mn atoms over Fe sites. The presence of two different components

Table 1. Summary of Refined Mössbauer Parameters Measured at 80 K: Centroid Shift, δ , Quadrupole Splitting, ϵ , Magnetic Hyperfine Field, B_{hf} , Line Width, Γ , and Intensity, I^a

component		MnFe ₂ O ₄	CoFe ₂ O ₄	NiFe ₂ O ₄
Fe ^{tetr.} :Fe ^{oct.}	parameter	45:55	47:53	34:66
Q ₁	δ_1 (mm s ⁻¹)	0.443	0.339	0.397
	ϵ_1 (mm s ⁻¹)	0.052	-0.016	0.015
	$B_{\text{hf}1}$ (mm s ⁻¹)	53.1	51.3	50.6
	Γ_1 (mm s ⁻¹)	0.22	0.37	0.38
	I_1 (%)	13	47	34
Q ₂	δ_2 (mm s ⁻¹)	0.415	0.507	0.488
	ϵ_2 (mm s ⁻¹)	0.049	-0.007	-0.009
	$B_{\text{hf}2}$ (mm s ⁻¹)	51.4	54.6	54.2
	Γ_2 (mm s ⁻¹)	0.31	0.27	0.34
	I_2 (%)	32	12	21
Q ₃	δ_3 (mm s ⁻¹)	0.514	0.428	0.474
	ϵ_3 (mm s ⁻¹)	-0.054	0.095	-0.136
	$B_{\text{hf}3}$ (mm s ⁻¹)	52.2	53.7	50.1
	Γ_3 (mm s ⁻¹)	0.27	0.22	0.31
	I_3 (%)	21	6	45
Q ₄	δ_4 (mm s ⁻¹)	0.509	0.573	
	ϵ_4 (mm s ⁻¹)	-0.068	-0.025	
	$B_{\text{hf}4}$ (mm s ⁻¹)	49.9	51.9	
	Γ_4 (mm s ⁻¹)	0.48	0.42	
	I_4 (%)	34	35	

^aTetrahedral Fe components (A site) are in bold.

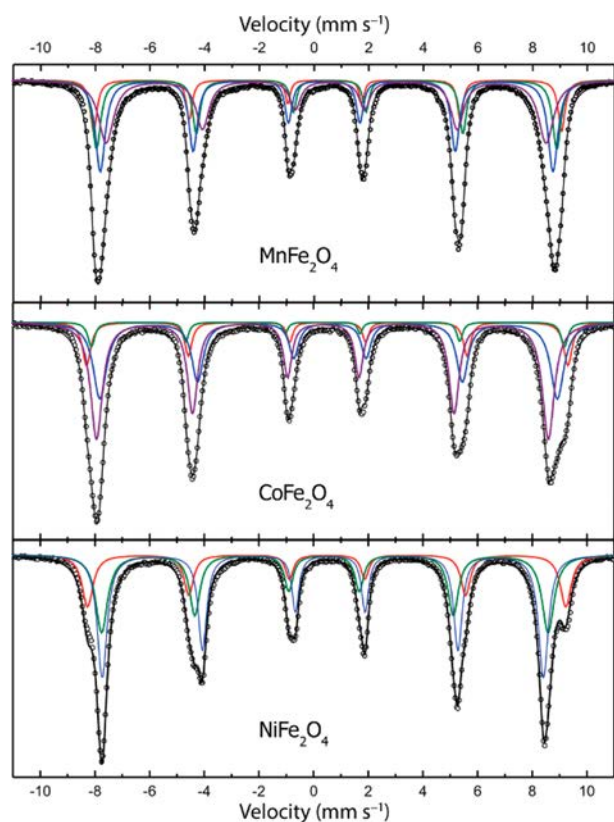


Figure 2. Mössbauer spectra for MFe₂O₄ (M = Mn, Co, Ni) ferrite NPs collected at 80 K. Experimental data: black circles. Calculated spectrum: black line. Q₁, Q₂, Q₃, and Q₄ components: red, blue, green, and violet, respectively.

for both tetrahedral and octahedral Fe sites indicates that there is a local preferential distribution of Mn atoms which creates different environments of neighboring Fe atoms.

CoFe₂O₄. The spectrum was fitted with four sextets, one for the A sites and three for the B sites. The tetrahedral Fe has the lowest chemical shift of 0.34 mm s⁻¹. In contrast to other TMs, Co is a “hard magnet”. In Co ferrite, there is a delicate balance between an increase of the B_{hf} values because of the presence of Co atoms as the nearest neighbors^{47,48} to both the A sites and the B sites and the decrease of the B_{hf} due to CME. The intensity for the Fe atoms in A sites is 47%, indicating an almost ideal composition of this inverse ferrite: (Co_{0.06}Fe_{0.94})^A[Co_{0.94}Fe_{1.06}]^BO₄. The Fe atoms in the octahedral site have three components with high centroid shifts and high hyperfine fields ($Q_4 = 51.9$ T). The reason for the presence of three components is not clear; however, the absence of the second component for tetrahedral iron indicates that the Fe/Co distribution is more random than the Fe/Mn one.

NiFe₂O₄. This spectrum was fitted with only three subspectra. The first component with a δ value around 0.40 mm s⁻¹ arises from Fe³⁺ in the A sites, while the other two components with higher δ values are the signals from Fe³⁺ in the B sites. Although Ni is a “soft magnet”, it increases the B_{hf} value slightly as the nearest neighbor.⁴⁹ The intensity of the A site component is 34%, resulting in the cation distributions being (Ni_{0.3}Fe_{0.7})^A[Ni_{0.7}Fe_{1.3}]^BO₄. It is noteworthy that this spectrum is somehow different from the spectra for the other two ferrite NPs. The overlap between the different sites is quite strong. Besides one of the components for B sites, which has the highest B_{hf} value, 54.2 T, the other component for the B sites is overlapping with the component for the A sites, resulting in strongly correlating intensities at this temperature. Measurement at RT indicates a higher intensity for A components, 42%, leading to (Ni_{0.2}Fe_{0.8})^A[Ni_{0.8}Fe_{1.2}]^BO₄ composition. In general, for Ni, the highest deviations from the ideal inverse ferrite composition were observed with a significant amount of Ni found to be in the tetrahedral A site. The Ni/Fe distribution is more random than the Fe/Mn distribution, since only one component for tetrahedral Fe is observed. In general, the large difference in size⁵⁰ between Mn and Fe may lead to some kind of ordered distribution, while Co and Ni are close in size to Fe and dispersed more randomly over the metal sublattice.

PDF. Three samples MFe₂O₄ with M = Fe, Ni, and Mn were analyzed by X-ray PDF. We have performed fitting in three structural models: the arystotype cubic spinel model in the $Fd-3m$ space group and two lower symmetry models in the $I4_1/amd$ and $P4_322$ space groups.

The least-squares PDF refinement in the $Fd-3m$ structural model provides a relatively good fit at high r -ranges; however, significant disagreements at low r -ranges (≤ 4 Å) are found (Figure 3). A plot of the low r -range (1–4 Å) is given to emphasize the local structure, where the M–O, M–M, and O–O pairing contributions are significant. The average structure model picks up the Fe–O peak at ~ 1.96 Å, and there is some broadening associated with this peak which corresponds to both tetrahedral and octahedral coordination environments. The expected Fe–O distances for typical Fe³⁺ with coordination numbers of 4, 5, and 6 are 1.865, 1.948, and 2.015 Å, respectively. The Fe–O distances here are 1.89 Å for the tetrahedral site and 2.04 Å for the octahedral site. Obviously, the average structure model underestimates the

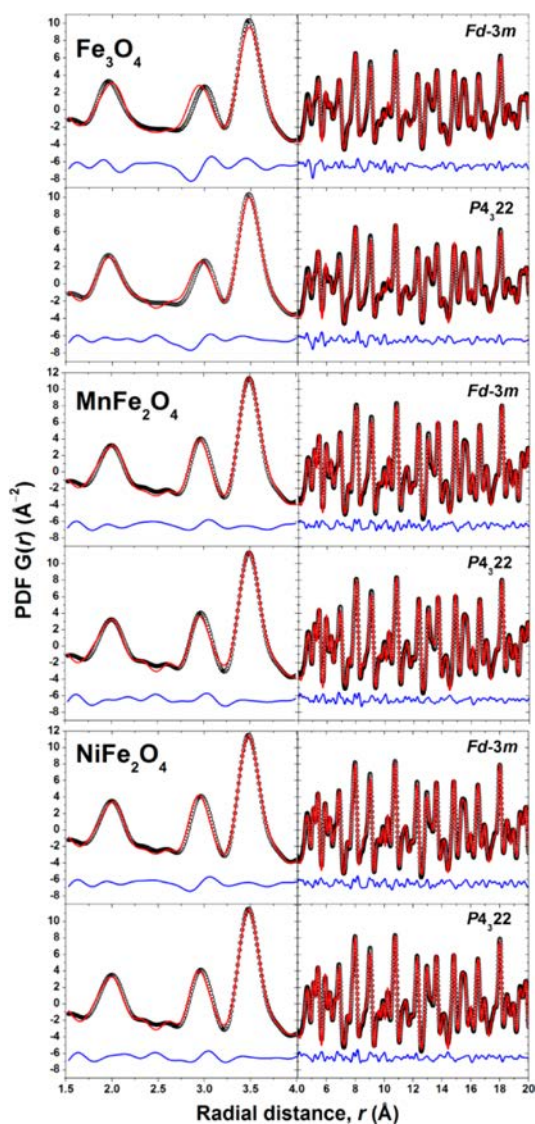


Figure 3. MnFe_2O_4 X-ray PDF fits for $r \leq 20$ Å in the $Fd-3m$ and $P4_322$ structural models. Experimental data, black circles; calculated spectrum, red line; difference, blue line.

clustered peak at 3.0 Å by ~ 0.05 Å, which corresponds to the O–O and Fe–Fe pairs (Figure 3). The refined spherical nanoparticle size was 7–9 nm, in good agreement with TEM data (Table S1, Supporting Information).

Refinement in the $I4_1/amd$ structural model has not improved the fit, and significantly higher disagreement factors were obtained. However, the $P4_322$ model describes the low r -range of Fe_3O_4 much better (Table S3, Figures S3–S4 (Supporting Information)). For the long range ($4 \text{ Å} < r < 20 \text{ Å}$), the improvement is moderate, thus indicating the local nature of the structural distortion.

MnFe_2O_4 and NiFe_2O_4 . Since Mn(Ni) and Fe have similar X-ray scattering factors, the metal site occupancy was not refined and fixed to the Mössbauer spectroscopy results. PDF refinement of MnFe_2O_4 and NiFe_2O_4 using the $Fd-3m$ model provides a relatively good fit at low and high r -ranges which is in contrast to the Fe_3O_4 material (Figure 3). The average structure model picks up the Mn(Ni)/Fe–O peak at ~ 2.0 Å, although there is a slight shift associated with the calculated pattern (~ 0.02 Å), and there is some broadening affiliated with

this peak, which corresponds to both tetrahedral and octahedral coordination environments. The M–O distances here are ~ 1.91 Å for the tetrahedral and 2.04 Å for the octahedral, roughly similar to Fe_3O_4 . Similarly to Fe_3O_4 but not as significant, the average structure model underestimates the clustered peak at 2.97 Å by ~ 0.02 Å, which corresponds to the O–O and M–M pairs. It seems that this shift is associated with the shift in the M–O peak at ~ 2.0 Å. The refined spherical nanoparticle size was 6–7 nm, which is consistent with TEM data (Table S1, Supporting Information).

Similar to the Fe_3O_4 case, the refinement in the $I4_1/amd$ structural model has not improved the fit and significantly higher disagreement factors were obtained. However, the $P4_322$ model describes the PDF of MnFe_2O_4 and NiFe_2O_4 better than the cubic model (Tables S5 and S8, Supporting Information). The improvements of the fits are more pronounced for the short range of r , indicating the local nature of the ordering.

Neutron PDF data were analyzed for four samples of MFe_2O_4 , M = Fe, Ni, Mn, and Co. Neutron refinements allow locating the oxygen atomic positions with higher precision. Rerefinement of the X-ray PDF data with oxygen positions fixed to the values obtained from neutron PDF refinements shows no substantial difference to the ones described above; therefore, these results were not included herein. Results of the neutron PDF refinements echo the X-ray PDF results: long-range data can be satisfactorily described with the cubic structural model, while the short-range data exhibit some deviation from the cubic symmetry and are better described in the tetragonal $P4_322$ structural model. The tetragonal structural distortion is more pronounced for the Fe_3O_4 NPs (Figure 4,

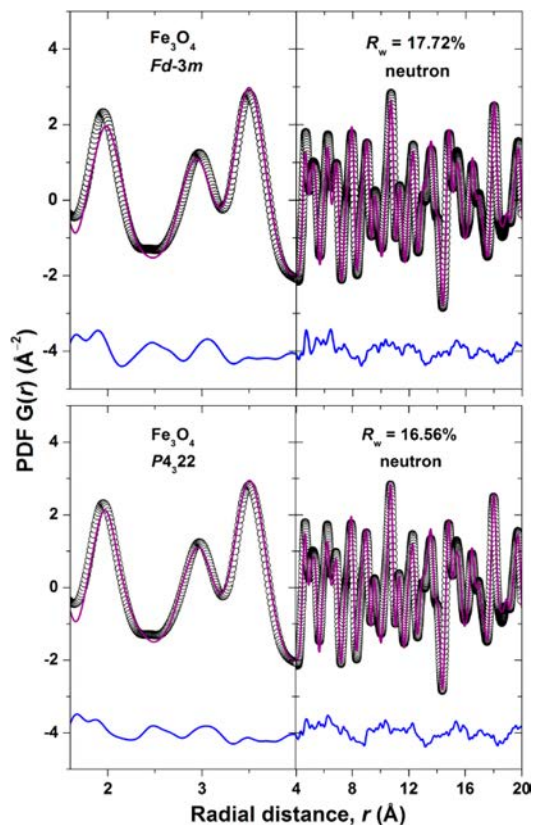


Figure 4. Fe_3O_4 neutron PDF fits for $r \leq 20$ Å in the $Fd-3m$ and $P4_322$ structural models. Experimental data, black circles; calculated spectrum, purple line; difference, blue line.

and Table S4, Figures S3-S4, Supporting Information) compared to MnFe_2O_4 NPs (Table S6, Figures S5-S6, Supporting Information), CoFe_2O_4 NPs (Table S7, Figures S7-S8, Supporting Information), and NiFe_2O_4 NPs (Table S9, Figures S9-S10, Supporting Information). The similarity of the neutron scattering lengths for Fe and Ni, 9.45 and 10.3 fm, did not allow the refinement of the Fe/Ni ratio in different crystallographic sites. In turn, the large difference in the neutron scattering lengths for Fe, Co, and Mn, 9.45, 2.49, and -3.73 fm, respectively, make possible refinements of the Fe/M ($M = \text{Co}$ and Mn) ratio in tetrahedral and octahedral sites in the structures of $\text{Co}(\text{or Mn})\text{Fe}_2\text{O}_4$. Free refinement of the Fe/Co ratio in both sites results in the $(\text{Co}_{0.35}\text{Fe}_{0.65(8)})^{\text{A}}[\text{Co}_{1.0}\text{Fe}_{1.0(2)}]^{\text{B}}\text{O}_4$ composition (Table S7, Supporting Information). The occupancies in the octahedral site are close to the results of Mössbauer spectroscopy, while neutron PDF indicates an excess of Co in the tetrahedral site. The refinement of the neutron PDF data with the composition of the tetrahedral site fixed to $\text{Co}_{0.1}\text{Fe}_{0.9}$ results in a similar fit as that for free refinement and 1:1 Co:Fe ratio in the octahedral site. For Mn, free refinement of the Fe/Mn ratio in both sites results in the $(\text{Mn}_{0.45}\text{Fe}_{0.55(5)})^{\text{A}}[\text{Mn}_{0.6}\text{Fe}_{1.4(7)}]^{\text{B}}\text{O}_4$ composition (Table S6, Supporting Information). The occupancies in both sites from neutron PDF indicate an excess of Mn, contradictory to the results of Mössbauer spectroscopy, which only show an excess of Mn in the octahedral site. These results should be taken with caution, as the data for MnFe_2O_4 were of not high enough quality to allow satisfactory fitting in any model (Figures S5 and S6, Supporting Information). The refinement of the neutron PDF data with the composition of the tetrahedral site fixed to $\text{Mn}_{0.1}\text{Fe}_{0.9}$ results in a poorer fit than that for the free refinement and nearly 1:1 Mn:Fe ratio in the octahedral site.

The PDF analyses point out that there are local distortions involved in these materials. We have tried to fit the data in two lower symmetry models, in $I4_1/amd$ and $P4_322$ space groups. The former model provides no improvements, while the latter one exhibits some improvement of the fit. In the $I4_1/amd$ spinel structure, there is one octahedral and one tetrahedral metal site. This model allows for the distortion of the local coordination from regular tetrahedron and octahedron, but still only one type of each polyhedron is present. In turn, in the $P4_322$ model, there are two different octahedral sites with different sets of $\text{M}^{\text{oct}}\text{-O}$ distances. Such tetragonal distortion was proposed on the basis of the ordering of the cations in the octahedral site.⁵¹ The possible reason for such distortion may be the significant excess of Fe^{3+} in the as-synthesized nanoparticles of Fe_3O_4 , as was shown in our previous works.^{22,42}

Mössbauer data indicates that for all studied ferrites there are two different octahedral sites with a nonuniform distribution of Fe atoms over those sites. This is consistent with the PDF results of the local $P4_322$ distortion, having two different octahedral sites.

A good measure of this local distortion was obtained from the comparison between the FWHM and peak center of the M–O (~ 2.0 Å) and M–M/O–O (~ 3.0 Å) pairing contributions (Table 2 and Figure 5). The FWHM for these peaks are nearly constant for all M; however, the bond distances (or peak maxima) are significantly different for $M = \text{Fe}$ and $M = \text{Mn, Co}$ or Ni . Similar results were obtained in the lower symmetry model in the $P4_322$ space group. All three fits were improved in this model, indicating distortion from the cubic symmetry. The drastic difference was obtained for $M =$

Table 2. Comparison of FWHM Obtained from X-ray and Neutron PDF Data of MFe_2O_4 ($M = \text{Fe, Mn, Co, Ni}$)^a

M	M–O FWHM	center (Å)	M–M/O–O FWHM	center (Å)
X-ray PDF				
Fe	0.239(6)	1.96962	0.213(3)	2.99218
Mn	0.242(3)	1.99731	0.211(3)	2.97003
Co				
Ni	0.240(3)	1.99143	0.220(3)	2.96168
Neutron PDF				
Fe	0.283(3)	1.95032	0.297(7)	2.9749
Mn	0.32(1)	1.94861	0.283(1)	2.97458
Co	0.31(1)	1.94552	0.295(6)	2.96409
Ni	0.29(1)	1.96637	0.276(7)	2.95548

^aThe values were obtained upon fitting each peak to a single Gaussian.

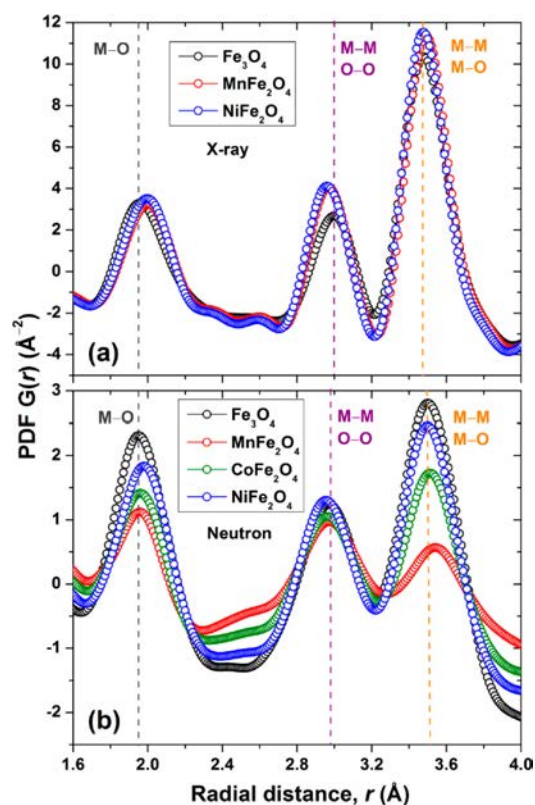


Figure 5. Fragments of the MFe_2O_4 ($M = \text{Fe, Mn, Co, and Ni}$) X-ray (a) and neutron (b) PDF patterns over r -range 1–4 Å.

Fe, while for $M = \text{Mn, Co, and Ni}$ the difference between the $Fd-3m$ and $P4_322$ was less pronounced. In general, these observations suggest that the structural solidarity of the tetrahedral and octahedral sites is significantly changed with chemical composition. As a result, it seems that the chemical substitution of M for Fe partially eliminates the local distortions. The complicated nature of the pristine Fe_3O_4 nanoparticles resulting from the excess of Fe^{3+} was recently observed by us using Mössbauer spectroscopy.⁴²

Electron Microscopy. TEM analysis of the as-synthesized samples reveals that all samples are in the size range of about 7–12 nm with reasonably narrow size distributions (Table S1 and Figure S11, Supporting Information). While nondoped magnetite NPs have an average diameter of 10.8 ± 3.1 nm, the size of doped NPs was found to decrease to around 7 nm with increasing nominal content of dopant (Table S1, Supporting

Information). The morphology of the NPs is close to spherical shape, although some triangular or octahedral shapes were also observed (Figure S12, Supporting Information).

As an example, Figure 6a shows an overview low-magnification TEM image of the $\text{Ni}_{0.15}\text{Fe}_{2.85}\text{O}_4$ NPs having a

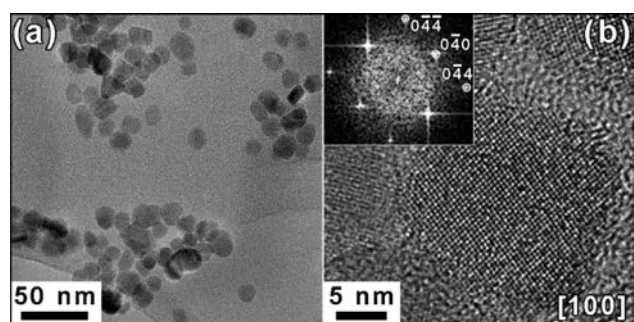


Figure 6. (a) Low-magnification TEM image of $\text{Ni}_{0.15}\text{Fe}_{2.85}\text{O}_4$ NPs. (b) [100] HRTEM image of the individual NP in the same sample, together with the corresponding FT pattern (inset), confirming cubic inverse-spinel-type crystal structure.

relatively narrow size distribution with an average diameter of 9.1 ± 3.6 nm (Table S1, Supporting Information), together with a HRTEM image of one of these NPs oriented along the [100] direction. A high crystallinity of the NPs is revealed in this image. The corresponding Fourier transform (FT) pattern shown as an inset in Figure 6b confirms the inverse-spinel-type structure, since it has been completely indexed on the basis of the Fe_3O_4 structure in the $Fd\bar{3}m$ space group using the unit cell parameter determined by XRD. No additional spots associated with secondary phases have been detected.

High-resolution HAADF-STEM images and the corresponding bright field (BF) STEM image of $\text{Ni}_{0.15}\text{Fe}_{2.85}\text{O}_4$ are shown in Figure 7a–c. The corresponding FT patterns prove that the NPs are ordered in a cubic structure (space group $Fd\bar{3}m$). The HAADF-STEM image (Figure 7a and b) shows a brighter contrast for the Fe/Ni atomic positions, and the weaker contrast corresponding to O positions. The O environment around the Fe/Ni is more clearly visible in the corresponding BF-STEM image (Figure 7c) as a smaller bright contrast around strong dark spots of the metal atom rows. Figure 7d shows the intensity profile along a column of atoms revealing the variation in the intensities of Fe/Ni and O atomic columns.

A high-resolution HAADF-STEM image of $\text{Ni}_{0.6}\text{Fe}_{2.4}\text{O}_4$ NP is shown in Figure 8a, which displays projections of Fe and Ni atomic columns, thus marking the high degree of crystallinity of the Ni-doped NPs. To confirm the element distribution of the synthesized $\text{M}_x\text{Fe}_{3-x}\text{O}_4$ NPs with different levels of doping, STEM-EDX and STEM-EELS elemental maps were recorded, which highlight the uniform distribution of Fe and O and random distribution of Ni within $\text{Ni}_{0.15}\text{Fe}_{2.85}\text{O}_4$ and $\text{Ni}_{0.6}\text{Fe}_{2.4}\text{O}_4$ NPs without clustering or formation of any phase-separated particles (Figures S13–S16, Supporting Information). The EDX spectrum obtained across a line scan of a representative sample reveals the presence of all elements (Fe, Ni, and O) in a single $\text{Ni}_{0.6}\text{Fe}_{2.4}\text{O}_4$ nanoparticle (Figure 8b). In addition, the incorporation of the Ni dopant into the structure was further confirmed by STEM-EDX line scan on an individual NP (Figure 8c). The line scan reveals the decrease in Fe signal (red line) and a corresponding increase in the Ni signal (green line), demonstrating that the doping of the Fe_3O_4

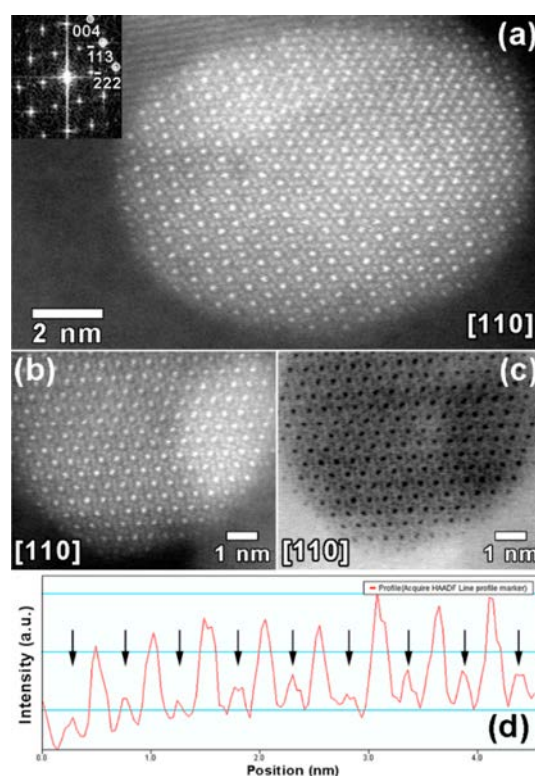


Figure 7. High-resolution HAADF-STEM (a, b) and BF-STEM (c) images of $\text{Ni}_{0.15}\text{Fe}_{2.85}\text{O}_4$ NPs in the [110] zone axis, together with the corresponding FT pattern (inset). (d) Intensity profile along the line of atomic columns of one NP in (c) showing the difference in the intensity due to the difference in the atomic number between Fe/Ni (larger peaks) and O (small peaks highlighted by the arrows).

NPs synthesized by hydrothermal methods is substitutional. During our STEM-EDX analysis, no evident signature of self-purification phenomenon,¹⁹ often present in doped semi-conducting nanocrystals, was observed.

Magnetic Properties. The magnetization versus magnetic field $M(H)$ dependences at RT are shown in Figure S17, Supporting Information, for all the samples. For Mn- and Ni-doped samples, a typical $M(H)$ dependence, characteristic of SPM, is observed independently of the metal-dopant content. However, in the case of Co doping, a progressive transition from SPM to FiM order with increased doping is observed. This is more clearly seen in the corresponding low-field region data plotted in Figure S18 (Supporting Information). Non-doped Fe_3O_4 NPs show SPM behavior, and SPM persists in the sample with the lowest level of doping $x = 0.06$ (Figure S18a and b, Supporting Information). Whereas coercive forces are absent for Ni- and Mn-doped samples, coercivity emerges upon alloying x from 0.15 to 1 in $\text{Co}_x\text{Fe}_{3-x}\text{O}_4$ (Figure S18c–g, Supporting Information). The observed development of the FiM at RT in $\text{Co}_x\text{Fe}_{3-x}\text{O}_4$ is attributed to the increasing magnetocrystalline anisotropy of magnetite NPs through Co incorporation.^{10,52} As a result, a larger coercive field is required to reverse the magnetization of the respective $\text{Co}_x\text{Fe}_{3-x}\text{O}_4$ NPs. We also note that the coercivity of the NPs increases when increasing Co concentration to $x = 0.6$ ($H_C = 317$ Oe), and decreases upon further increase in Co concentration (Figure 9a). The initial increase in coercivity is associated with the enhancement of magnetic anisotropy with increasing Co concentration. The subsequent decrease is a surprising result.

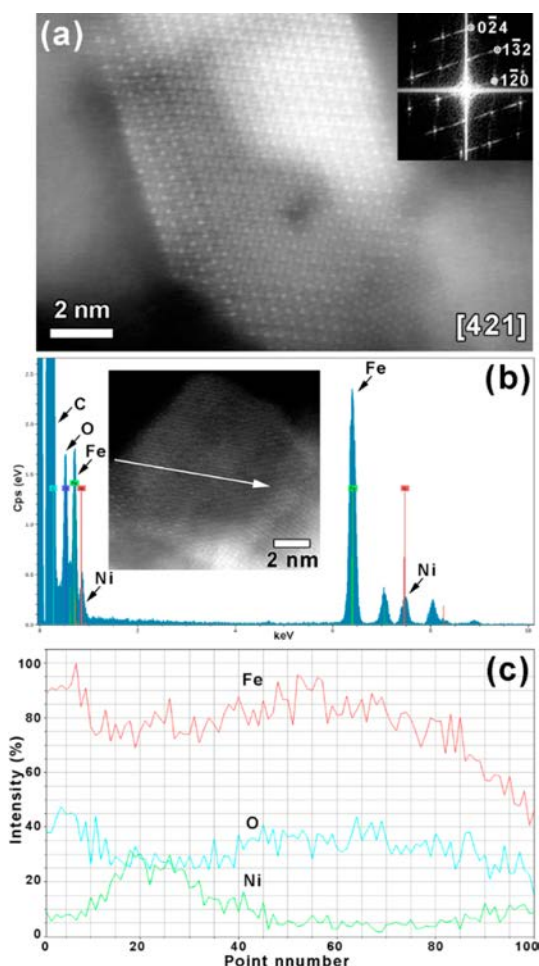


Figure 8. (a) A high-resolution HAADF-STEM image of a single $\text{Ni}_{0.6}\text{Fe}_{2.4}\text{O}_4$ NP in the [421] zone axis, together with the corresponding FT pattern (inset). (b) STEM-EDX spectrum of $\text{Ni}_{0.6}\text{Fe}_{2.4}\text{O}_4$ NP (inset), demonstrating the presence of all the expected elements in the single NP. (c) STEM-EDX line scan through an individual $\text{Ni}_{0.6}\text{Fe}_{2.4}\text{O}_4$ NP (indicated by the arrow in the inset in b), revealing the presence of Fe, Ni, and O.

One possible explanation is that Fe–Co interactions are responsible for the increase in magnetic anisotropy while Co–Co interactions at high Co content reduce the anisotropy. AFM interparticle interactions may also be responsible for the observed decrease of coercivity.⁵³

In general, for temperatures, T , higher than the blocking temperature, T_B , the sample is in the superparamagnetic state, and thus, no hysteresis or coercivity will be present. For temperatures below T_B , the sample will appear magnetically ordered exhibiting hysteresis and coercivity. Studies exploring interparticle interactions in magnetic systems have proposed that T_B for a particle of volume V is determined according to eq 1^{54,55}

$$T_B = T_0 + [T_a / \ln(f_0 / f_m)] \quad (1)$$

where $T_a = K_{\text{an}}V/k_B$ with k_B and K_{an} being the Boltzmann and anisotropy constants, respectively, f_0 and f_m are the attempt and measuring frequencies, respectively, and T_0 is the strength of interparticle interactions. Notably, the time scales of the Mössbauer spectroscopy and vibrating sample magnetometry are different. In particular, for Mössbauer studies $f_m \approx 10^{10}$ Hz, whereas for vibrating sample magnetometry $f_m \approx 10$ Hz.

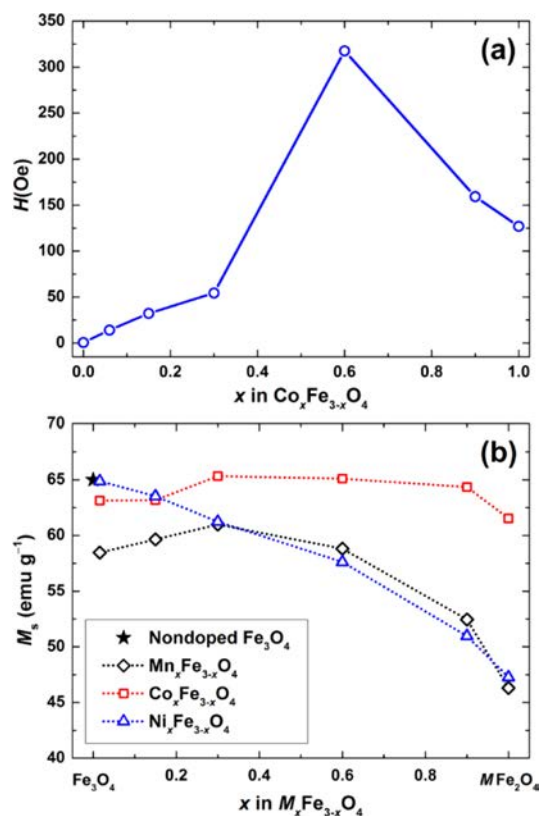


Figure 9. (a) Coercivity H_C as a function of x in $\text{Co}_x\text{Fe}_{3-x}\text{O}_4$ NPs. (b) Composition x dependence of the saturation magnetization M_s of $\text{M}_x\text{Fe}_{3-x}\text{O}_4$ NPs. The solid and dotted lines are guides for the eye.

Therefore, the blocking temperature estimated from Mössbauer studies will be considerably higher than that coming from vibrating sample magnetometry, when all other parameters are kept unchanged.⁵⁶ Accordingly, the magnetic order in ferrite NPs found at RT in Mössbauer studies (Supporting Information) may not be detected by vibrating sample magnetometry.

Our $M(H)$ data demonstrate that all the colloidal $\text{M}_x\text{Fe}_{3-x}\text{O}_4$ NPs except those of the $\text{Co}_x\text{Fe}_{3-x}\text{O}_4$ series are superparamagnetic at RT (Figure S17, Supporting Information). Since the anisotropy constant for Co is much higher than that for Ni and Mn,¹⁰ following eq 1, the blocking temperature for Co-doped magnetite may be above RT, thus providing a plausible explanation for the observation of ferrimagnetism in $\text{Co}_x\text{Fe}_{3-x}\text{O}_4$ NPs. On the other hand, the blocking temperature for Ni- and Mn-doped magnetite may be below RT, resulting in the lack of coercivity at this temperature for $\text{Mn}_x\text{Fe}_{3-x}\text{O}_4$ and $\text{Ni}_x\text{Fe}_{3-x}\text{O}_4$ NPs.

To corroborate these assumptions and confirm the observed RT $M(H)$ behavior, the T_B values for the end member ferrites were estimated from the zero-field-cooling (ZFC) and field-cooling (FC) magnetization curves recorded using a SQUID-VSM magnetometer. As shown in Figure S19 (Supporting Information), while blocking temperatures for Fe_3O_4 and CoFe_2O_4 are well above 300 K, those for MnFe_2O_4 and NiFe_2O_4 are observed below 300 K with estimated values of about 110 and 185 K, respectively. Furthermore, we also recorded the $M(H)$ data for the end member ferrites at 2 K, a temperature well below T_B (Figure S20, Supporting Information). As expected, the hysteresis loops are pronounced in all cases, indicating that the low temperatures enable ferrimagnetic

interaction in the samples due to the magnetic ordering below blocking temperature. Overall, the data suggests that blocking temperatures below RT are most likely responsible for the observed superparamagnetic behavior of Mn- and Ni-doped magnetite NPs at RT. On the other hand, the larger K_{an} in the $\text{Co}_x\text{Fe}_{3-x}\text{O}_4$ series induces an increase of the coercivity and remanence in the $M(H)$ curves at RT upon alloying. It is also important to note that, due to the fact that NPs were used in the magnetic measurements, we cannot rule out whether additional finite-size effects and associated thermal relaxation also play a role in the development of superparamagnetism above blocking temperature.^{4,57}

Saturation magnetization M_s has been obtained by extrapolating M versus $1/H$ for $1/H \rightarrow 0$, and the estimated values are plotted in Figure 9b. In all cases, the magnetization has been normalized to the total sample mass, which includes the magnetic core and the organic protective shell around the NPs (typically ca. 10–15%).²² M_s values obtained for the NPs are slightly lower than those of the corresponding bulk materials ($M_s(\text{Fe}_3\text{O}_4) = 82 \text{ emu g}^{-1}$; $M_s(\text{MnFe}_2\text{O}_4) = 110 \text{ emu g}^{-1}$; $M_s(\text{CoFe}_2\text{O}_4) = 94 \text{ emu g}^{-1}$; $M_s(\text{NiFe}_2\text{O}_4) = 56 \text{ emu g}^{-1}$),⁵⁸ which is mainly due to an overestimation of the mass of the samples as a consequence of the presence of organic coating, reduced particle size, and surface anisotropy.⁴ We observed that M_s is the highest for the nondoped Fe_3O_4 ($\sim 65 \text{ emu g}^{-1}$), and then decreases with increasing Mn and Ni dopant concentrations (Figure 9b). A notable decrease is observed as the end members MnFe_2O_4 and NiFe_2O_4 are approached ($\sim 45 \text{ emu g}^{-1}$). In the case of Co doping (Figure 9b), the change in M_s is found to be moderate ($\sim 62 \text{ emu g}^{-1}$ for CoFe_2O_4).

It is well-known that the saturation magnetization of magnetic materials is generally size dependent at the nanoscale.⁵⁷ The fact that the size of the as-synthesized NPs slightly decreases with increasing dopant concentration (Table S1, Supporting Information) suggests that in our colloidal $\text{M}_x\text{Fe}_{3-x}\text{O}_4$ NPs the variation in M_s is partially due to the size change. However, $\text{Mn}_x\text{Fe}_{3-x}\text{O}_4$ and $\text{Ni}_x\text{Fe}_{3-x}\text{O}_4$ ($x = 0.6, 0.9, 1$) NPs exhibit a significant decrease of M_s within the series with increasing x despite having similar particle size (Table S1, Supporting Information; Figure 9b), indicating that the saturation magnetization of the doped NPs is not solely determined by their size. Therefore, the observed significant decrease in M_s with doping highlights the important role played by chemical composition. Specifically, Mn and Ni substitution appears to suppress M_s of magnetite, while Co substitution does not affect M_s (Figure 9b). The reduction of M_s for high doping levels is most likely a result of the different site occupancy of metal cations in A or B sublattices, which are responsible for the relative contribution of superexchange or exchange interaction ratios,⁵⁹ judging from the decreased magnetic moment of the end member compounds.⁶⁰

4. CONCLUDING REMARKS

The present study has demonstrated that a series of doped magnetite nanoparticles $\text{M}_x\text{Fe}_{3-x}\text{O}_4$ ($M = \text{Mn, Co, Ni}$; $x = 0, 0.06, 0.15, 0.3, 0.6, 0.9, \text{ and } 1$) can be prepared using a simple hydrothermal reaction in aqueous medium and at a considerably lower reaction temperature ($200 \text{ }^\circ\text{C}$) than in previously reported syntheses in organic solvents. Oleate-capped and, thus, solvent dispersible nanoparticles having relatively narrow size distributions are formed. It was found that the mean size of the particles is rather insensitive to the

chemical composition, suggesting that, in the current synthesis protocol, doping has no significant influence on the crystal growth process. Further, our investigation of the doped nanoparticles with a set of complementary techniques provides evidence that the dopants do not form a separate crystalline or amorphous phase but fully dissolve in the inverse-spinel structure of magnetite, yielding a solid solution $\text{M}_x\text{Fe}_{3-x}\text{O}_4$ with stoichiometric ferrites as the end members. Moreover, from detailed Raman spectroscopy studies, we found a strong influence of Mn doping on the host magnetite matrix, as reflected by a significant red-shift of the principal A_{1g} phonon mode. Our Mössbauer spectroscopy study of the end member ferrite NPs shows that all iron atoms have Fe^{3+} oxidation state, indicating that the TM dopants have M^{2+} oxidation state. Existence of two different components in the Mössbauer spectrum of MnFe_2O_4 NPs representing tetrahedral and octahedral Fe sites is interpreted as a result of the fine structure of the ferrite with possible Fe/Mn ordering. In contrast, CoFe_2O_4 and NiFe_2O_4 exhibit a non-ordered M/Fe distribution with Co preferentially in octahedral sites and Ni in both octahedral and tetrahedral sites. PDF analysis demonstrates that the local structure of nondoped Fe_3O_4 NPs is distorted and the local distortions can be eliminated to a large extent via Mn and Ni atoms substituting Fe. The HRTEM, HAADF-STEM, STEM-EDX, and STEM-EELS investigations revealed a single-phase structure of $\text{M}_x\text{Fe}_{3-x}\text{O}_4$ with uniform (Fe, O) and random (Ni) distributions of the constituent elements within individual nanoparticles. The latter fact implies that the doped nanoparticles do not demonstrate a self-purification phenomenon, which is typically observed in semiconducting nanocrystals.

We have shown that there is a direct correlation between the magnetic properties and chemical composition of the $\text{M}_x\text{Fe}_{3-x}\text{O}_4$ nanoparticles. In particular, the measured room temperature saturation magnetization of Co-doped samples is similar or slightly lower compared to that of nondoped Fe_3O_4 , while doping of Fe_3O_4 with Mn and Ni leads to a significant decrease in the saturation magnetization. Furthermore, room temperature hysteresis data for all the samples indicate that magnetite nanoparticles develop ferrimagnetic behavior upon Co doping, whereas for Mn and Ni doping superparamagnetic behavior is preserved. Our SQUID experiments reveal that superparamagnetism of $\text{Mn}_x\text{Fe}_{3-x}\text{O}_4$ and $\text{Ni}_x\text{Fe}_{3-x}\text{O}_4$ NPs at room temperature most likely stems from the fact that their blocking temperatures are lower than the room temperature. In conclusion, the present findings improve current capabilities to synthesize doped colloidal nanocrystals, and show that doping is a toolbox for the design and preparation of nanomaterials with modified and new properties.

■ ASSOCIATED CONTENT

Supporting Information

Additional synthesis, characterization, Mössbauer spectroscopy, pair distribution function analysis, electron microscopy, and magnetic properties data. The Supporting Information is available free of charge on the ACS Publications website at DOI: 10.1021/acs.jpcc.5b01575.

■ AUTHOR INFORMATION

Corresponding Author

*E-mail: yury.kolenko@inl.int.

Notes

The authors declare no competing financial interest.

ACKNOWLEDGMENTS

We are thankful to Dr. L. M. Salonen and Prof. P. Freitas (both INL) for helpful discussions, as well as to the manuscript reviewers for providing useful comments on the manuscript. We would also like to thank the ORNL NOMAD mail-in program (Proposal ID IPTS-10113) and, specifically, Dr. J. Neuefeind and Dr. M. Feygenson for the collection of PDF data. This work has benefited from the financial support provided by the ERDF (ON.2 - O Novo Norte Program), EU FP7 Cooperation Programme through NMP-theme (Grant No. 314212), and InveNNTa project financed by EU Programme for Cross-border Cooperation: Spain-Portugal. Research conducted at ORNL's Spallation Neutron Source was sponsored by the Scientific User Facilities Division, Office of Basic Energy Sciences, U.S. Department of Energy. Use of the Advanced Photon Source at Argonne National Laboratory was supported by the U.S. Department of Energy, Office of Science, Office of Basic Energy Sciences, under Contract No. DE-AC02-06CH11357. The Mössbauer facility was supported by NIH (Grant No. 1S10RR023656-01A1). E.C.-A. acknowledges the I2C Plan (Xunta de Galicia, Spain) for a postdoctoral fellowship.

REFERENCES

- (1) Cornell, R. M.; Schwertmann, U. *The Iron Oxides: Structure, Properties, Reactions, Occurrences and Uses*, 2nd ed.; Wiley-VCH: Weinheim, Germany, 2003.
- (2) Verwey, E. J. W. Electronic Conduction of Magnetite (Fe_3O_4) and Its Transition Point at Low Temperatures. *Nature* **1939**, *144*, 327–328.
- (3) Senn, M. S.; Wright, J. P.; Atfield, J. P. Charge Order and Three-Site Distortions in the Verwey Structure of Magnetite. *Nature* **2012**, *481*, 173–176.
- (4) Krishnan, K. M. Biomedical Nanomagnetism: A Spin through Possibilities in Imaging, Diagnostics, and Therapy. *IEEE Trans. Magn.* **2010**, *46*, 2523–2558.
- (5) Gao, J. H.; Gu, H. W.; Xu, B. Multifunctional Magnetic Nanoparticles: Design, Synthesis, and Biomedical Applications. *Acc. Chem. Res.* **2009**, *42*, 1097–1107.
- (6) Dupuis, C.; Beaudoin, G. Discriminant Diagrams for Iron Oxide Trace Element Fingerprinting of Mineral Deposit Types. *Miner. Deposita* **2011**, *46*, 319–335.
- (7) Neel, L. Propriétés Magnétiques Des Ferrites - Ferrimagnétisme Et Antiferromagnétisme. *Ann. Phys. Paris* **1948**, *3*, 137–198.
- (8) Hastings, J. M.; Corliss, L. M. Neutron Diffraction Study of Manganese Ferrite. *Phys. Rev.* **1956**, *104*, 328–331.
- (9) Takaobushi, J.; et al. Electronic Structures of $\text{Fe}_{(3-x)}\text{M}_{(x)}\text{O}_4$ ($M = \text{Mn}, \text{Zn}$) Spinel Oxide Thin Films Investigated by X-Ray Photoemission Spectroscopy and X-Ray Magnetic Circular Dichroism. *Phys. Rev. B* **2007**, *76*, 205108.
- (10) Tripathy, D.; Adeyeye, A. O.; Boothroyd, C. B.; Piramanayagam, S. N. Magnetic and Transport Properties of Co-Doped Fe_3O_4 Films. *J. Appl. Phys.* **2007**, *101*, 013904.
- (11) He, Z.; Koza, J. A.; Mu, G. J.; Miller, A. S.; Bohannon, E. W.; Switzer, J. A. Electrodeposition of $\text{Co}_x\text{Fe}_{3-x}\text{O}_4$ Epitaxial Films and Superlattices. *Chem. Mater.* **2013**, *25*, 223–232.
- (12) Moyer, J. A.; Vaz, C. A. F.; Negusse, E.; Arena, D. A.; Henrich, V. E. Controlling the Electronic Structure of $\text{Co}_{1-x}\text{Fe}_{2+x}\text{O}_4$ Thin Films through Iron Doping. *Phys. Rev. B* **2011**, *83*, 035121.
- (13) Chou, C. Y.; Kuo, P. C.; Yao, Y. D.; Sun, A. C.; Fang, Y. H.; Chen, S. C.; Huang, C. H.; Chen, J. W. Effects of Sintering Temperature on the Magnetoresistance and Microstructure of the Mixture of Fe_3O_4 and Cu-Ferrite Powder. *IEEE Trans. Magn.* **2005**, *41*, 2757–2759.
- (14) Salazar-Alvarez, G.; Olsson, R. T.; Sort, J.; Macedo, W. A. A.; Ardisson, J. D.; Baro, M. D.; Gedde, U. W.; Nogues, J. Enhanced Coercivity in Co-Rich near-Stoichiometric $\text{CoFe}_{3-x}\text{O}_{4+\delta}$ Nanoparticles Prepared in Large Batches. *Chem. Mater.* **2007**, *19*, 4957–4963.
- (15) Lee, J. H.; et al. Artificially Engineered Magnetic Nanoparticles for Ultra-Sensitive Molecular Imaging. *Nat. Med.* **2007**, *13*, 95–99.
- (16) Buonsanti, R.; Milliron, D. J. Chemistry of Doped Colloidal Nanocrystals. *Chem. Mater.* **2013**, *25*, 1305–1317.
- (17) Norris, D. J.; Efros, A. L.; Erwin, S. C. Doped Nanocrystals. *Science* **2008**, *319*, 1776–1779.
- (18) Erwin, S. C.; Zu, L. J.; Haftel, M. I.; Efros, A. L.; Kennedy, T. A.; Norris, D. J. Doping Semiconductor Nanocrystals. *Nature* **2005**, *436*, 91–94.
- (19) Mikulec, F. V.; Kuno, M.; Bennati, M.; Hall, D. A.; Griffin, R. G.; Bawendi, M. G. Organometallic Synthesis and Spectroscopic Characterization of Manganese-Doped CdSe Nanocrystals. *J. Am. Chem. Soc.* **2000**, *122*, 2532–2540.
- (20) Jang, J. T.; Nah, H.; Lee, J. H.; Moon, S. H.; Kim, M. G.; Cheon, J. Critical Enhancements of MRI Contrast and Hyperthermic Effects by Dopant-Controlled Magnetic Nanoparticles. *Angew. Chem., Int. Ed.* **2009**, *48*, 1234–1238.
- (21) Lee, J.; Zhang, S.; Sun, S. H. High-Temperature Solution-Phase Syntheses of Metal-Oxide Nanocrystals. *Chem. Mater.* **2013**, *25*, 1293–1304.
- (22) Kolen'ko, Y. V.; et al. Large-Scale Synthesis of Colloidal Fe_3O_4 Nanoparticles Exhibiting High Heating Efficiency in Magnetic Hyperthermia. *J. Phys. Chem. C* **2014**, *118*, 8691–8701.
- (23) Akselrud, L. G.; Zavalii, P. Y.; Grin, Y. N.; Pecharsky, V. K.; Baumgartner, B.; Wolfel, E. Use of the CSD Program Package for Structure Determination from Powder Data. *Mater. Sci. Forum* **1993**, *133–136*, 335–340.
- (24) Lagarec, K.; Rancourt, D. C. *Recoil, Mössbauer Spectral Analysis Software for Windows, 1.0*; University of Ottawa: Ottawa, Canada, 1998.
- (25) Farrow, C. L.; Juhas, P.; Liu, J. W.; Bryndin, D.; Bozin, E. S.; Bloch, J.; Proffen, T.; Billinge, S. J. L. PDFfit2 and PDFgui: Computer Programs for Studying Nanostructure in Crystals. *J. Phys.: Condens. Matter* **2007**, *19*, 335219.
- (26) Taniguchi, T.; Nakagawa, K.; Watanabe, T.; Matsushita, N.; Yoshimura, M. Hydrothermal Growth of Fatty Acid Stabilized Iron Oxide Nanocrystals. *J. Phys. Chem. C* **2009**, *113*, 839–843.
- (27) Hong, J. H.; Kim, W. S.; Lee, J. I.; Hur, N. H. Exchange Coupled Magnetic Nanocomposites of $\text{Sm}(\text{Co}_{1-x}\text{Fe}_x)_5/\text{Fe}_3\text{O}_4$ with Core/Shell Structure. *Solid State Commun.* **2007**, *141*, 541–544.
- (28) Gu, Z. J.; Xiang, X.; Fan, G. L.; Li, F. Facile Synthesis and Characterization of Cobalt Ferrite Nanocrystals Via a Simple Reduction-Oxidation Route. *J. Phys. Chem. C* **2008**, *112*, 18459–18466.
- (29) Shoemaker, D. P.; Li, J.; Seshadri, R. Unraveling Atomic Positions in an Oxide Spinel with Two Jahn-Teller Ions: Local Structure Investigation of CuMn_2O_4 . *J. Am. Chem. Soc.* **2009**, *131*, 11450–11457.
- (30) Shoemaker, D. P.; Seshadri, R. Total-Scattering Descriptions of Local and Cooperative Distortions in the Oxide Spinel $\text{Mg}_{1-x}\text{Cu}_x\text{Cr}_2\text{O}_4$ with Dilute Jahn-Teller Ions. *Phys. Rev. B* **2010**, *82*, 214107.
- (31) Shebanova, O. N.; Lazor, P. Raman Spectroscopic Study of Magnetite (FeFe_2O_4): A New Assignment for the Vibrational Spectrum. *J. Solid State Chem.* **2003**, *174*, 424–430.
- (32) Verbe, J. L. Temperature-Dependent Light-Scattering Studies of Verwey Transition and Electronic Disorder in Magnetite. *Phys. Rev. B* **1974**, *9*, 5236–5248.
- (33) Jubb, A. M.; Allen, H. C. Vibrational Spectroscopic Characterization of Hematite, Maghemite, and Magnetite Thin Films Produced by Vapor Deposition. *ACS Appl. Mater. Interfaces* **2010**, *2*, 2804–2812.
- (34) Jacintho, G. V. M.; Brolo, A. G.; Corio, P.; Suarez, P. A. Z.; Rubim, J. C. Structural Investigation of MFe_2O_4 ($M = \text{Fe}, \text{Co}$) Magnetic Fluids. *J. Phys. Chem. C* **2009**, *113*, 7684–7691.

- (35) Ahlawat, A.; Sathe, V. G. Raman Study of NiFe₂O₄ Nanoparticles, Bulk and Films: Effect of Laser Power. *J. Raman Spectrosc.* **2011**, *42*, 1087–1094.
- (36) Lazarevic, Z. Z.; Jovalekic, C.; Milutinovic, A.; Romcevic, M. J.; Romcevic, N. Z. Preparation and Characterization of Nano Ferrites. *Acta Phys. Polym., A* **2012**, *121*, 682–686.
- (37) Yamashita, O.; Ikeda, T. Effect of Polishing Stress on Raman Spectra of the Mn-Zn Ferrite. *J. Appl. Phys.* **2004**, *95*, 1743–1748.
- (38) Julien, C.; Massot, M.; Rangan, S.; Lemal, M.; Guyomard, D. Study of Structural Defects in γ -MnO₂ by Raman Spectroscopy. *J. Raman Spectrosc.* **2002**, *33*, 223–228.
- (39) Ramana, C. V.; Massot, M.; Julien, C. M. Xps and Raman Spectroscopic Characterization of LiMn₂O₄ Spinels. *Surf. Interface Anal.* **2005**, *37*, 412–416.
- (40) Varshney, D.; Verma, K.; Kumar, A. Structural and Vibrational Properties of Zn_xMn_{1-x}Fe₂O₄ ($x = 0.0, 0.25, 0.50, 0.75, 1.0$) Mixed Ferrites. *Mater. Chem. Phys.* **2011**, *131*, 413–419.
- (41) Sawatzky, G. A.; Vanderwo, F.; Morrish, A. H. Mössbauer Study of Several Ferrimagnetic Spinels. *Phys. Rev.* **1969**, *187*, 747.
- (42) Kolen'ko, Y. V.; et al. High-Temperature Magnetism as a Probe for Structural and Compositional Uniformity in Ligand-Capped Magnetite Nanoparticles. *J. Phys. Chem. C* **2014**, *118*, 28322–28329.
- (43) Mørup, S.; Madsen, D. E.; Frandsen, C.; Bahl, C. R. H.; Hansen, M. F. Experimental and Theoretical Studies of Nanoparticles of Antiferromagnetic Materials. *J. Phys.: Condens. Matter* **2007**, *19*, 213202.
- (44) Mørup, S.; Topsoe, H. Mössbauer Studies of Thermal Excitations in Magnetically Ordered Microcrystals. *Appl. Phys.* **1976**, *11*, 63–66.
- (45) Chen, J. P.; Sorensen, C. M.; Klabunde, K. J.; Hadjipanayis, G. C.; Devlin, E.; Kostikas, A. Size-Dependent Magnetic Properties of MnFe₂O₄ Fine Particles Synthesized by Coprecipitation. *Phys. Rev. B* **1996**, *54*, 9288–9296.
- (46) Morrish, A. H.; Clark, P. E. High-Field Mössbauer Study of Manganese-Zinc Ferrites. *Phys. Rev. B* **1975**, *11*, 278–286.
- (47) Kamali, S.; Haggstrom, L.; Sahlberg, M.; Wappling, R. Magnetic and Interface Properties of Fe_{0.82}Ni_{0.18}/Co(001) Superlattices. *J. Phys.: Condens. Matter* **2011**, *23*, 055301.
- (48) Kamali, S. M.; Bergman, A.; Andersson, G.; Stanciu, V.; Haggstrom, L. Local Magnetic Effects of Interface Alloying in Fe/Co Superlattices. *J. Phys.: Condens. Matter* **2006**, *18*, 5807–5824.
- (49) Kamali, S. M.; Blixt, A. M.; Haggstrom, L.; Wappling, R.; Stanciu, V.; Nordblad, P. Magnetic Properties of a Fe_{0.82}Ni_{0.18}/V(001) Superlattice Studied by Mössbauer Spectroscopy. *J. Magn. Magn. Mater.* **2004**, *272*, 1263–1265.
- (50) Shannon, R. D. Revised Effective Ionic-Radii and Systematic Studies of Interatomic Distances in Halides and Chalcogenides. *Acta Crystallogr., Sect. A* **1976**, *32*, 751–767.
- (51) Haas, C. Phase Transitions in Crystals with Spinel Structure. *J. Phys. Chem. Solids* **1965**, *26*, 1225–1232.
- (52) Sytnyk, M.; et al. Tuning the Magnetic Properties of Metal Oxide Nanocrystal Heterostructures by Cation Exchange. *Nano Lett.* **2013**, *13*, 586–593.
- (53) Mørup, S.; Hansen, M. F.; Frandsen, C. Magnetic Interactions between Nanoparticles. *Beilstein J. Nanotechnol.* **2010**, *1*, 182–190.
- (54) Chantrell, R. W.; Walmsley, N.; Gore, J.; Maylin, M. Calculations of the Susceptibility of Interacting Superparamagnetic Particles. *Phys. Rev. B* **2001**, *63*, 024410.
- (55) Singh, V.; Seehra, M. S.; Bonevich, J. Ac Susceptibility Studies of Magnetic Relaxation in Nanoparticles of Ni Dispersed in Silica. *J. Appl. Phys.* **2009**, *105*, 07B518.
- (56) Mørup, S. Superparamagnetism and Spin-Glass Ordering in Magnetic Nanocomposites. *Europhys. Lett.* **1994**, *28*, 671–676.
- (57) Dutta, P.; Pai, S.; Seehra, M. S.; Shah, N.; Huffman, G. P. Size Dependence of Magnetic Parameters and Surface Disorder in Magnetite Nanoparticles. *J. Appl. Phys.* **2009**, *105*, 07B501.
- (58) Carta, D.; Casula, M. F.; Falqui, A.; Loche, D.; Mountjoy, G.; Sangregorio, C.; Corrias, A. A Structural and Magnetic Investigation of the Inversion Degree in Ferrite Nanocrystals MFe₂O₄ ($M = \text{Mn, Co, Ni}$). *J. Phys. Chem. C* **2009**, *113*, 8606–8615.
- (59) Franco, A.; Silva, F. C. E. Effect of the Zn Content in the Magnetic Properties of Co_{1-x}Zn_xFe₂O₄ Mixed Ferrites. *J. Appl. Phys.* **2013**, *113*, 17B513.
- (60) Szotek, Z.; Temmerman, W. M.; Kodderitzsch, D.; Svane, A.; Petit, L.; Winter, H. Electronic Structures of Normal and Inverse Spinel Ferrites from First Principles. *Phys. Rev. B* **2006**, *74*, 174431.